



Contents lists available at ScienceDirect

Chemical Engineering Journal

journal homepage: www.elsevier.com/locate/cej

Catalyst screening and reaction kinetics of liquid phase DME synthesis under reactive distillation conditions

M. Semmel^a, L. Steiner^a, M. Bontrup^a, J. Sauer^b, O. Salem^{a,*}^a Fraunhofer-Institute for Solar Energy Systems ISE, Heidenhofstr. 2, 79110 Freiburg, Germany^b Karlsruhe Institute of Technology (KIT), Hermann-von-Helmholtz-Platz 1, D-76344 Eggenstein-Leopoldshafen, Germany

ARTICLE INFO

Keywords:

Dimethyl ether: DME
Kinetic measurements
Kinetic model
Ion exchange resin
Power-to-DME
Reactive distillation

ABSTRACT

While conventional DME synthesis is exclusively operated in a gas phase heterogenous reaction system, reactive distillation unveils the potential for a process intensified, compact and efficient DME production. In a catalyst screening, various solid acid catalysts were examined in the liquid phase dehydration of methanol to DME. Ion exchange resins proved to be more active than zeolites and more stable than perfluorsulfonic acids. Reaction kinetics on the two most promising commercial ion exchange resins, the oversulfonated resin Amberlyst® 36 and the chlorinated resin Treverlyst CAT400 were studied in a profile reactor setup over the full range of water fractions relevant for DME reactive distillation processes. CAT 400 was found to show a lower activity than Amberlyst® 36 at identical temperatures, however, due to the higher thermal stability, significantly higher conversions could be achieved. In the kinetic fitting, it was found that the conventional Eley-Rideal and Langmuir-Hinshelwood mechanisms are not capable to describe the experimental data over the wide range of water fractions due to the highly non-linear inhibition by water resulting from the distinct swelling properties of ion exchange resins. To account for this behavior, a new kind of kinetic model with dedicated water inhibition term is introduced and discussed. This model allows the precise description of reaction kinetics over the whole studied operating range for both investigated catalysts and reflects the temperature-dependent inhibition by water. The new kinetic model is an essential building block for the design of industrial scale DME reactive distillation processes.

1. Introduction

The ever-growing greenhouse gas emissions since the industrial revolution are the major reason for the anthropogenic climate change and its severe consequences, necessitating mankind to shift from a fossil-based to a carbon neutral economy based on renewable power generation. However, the geographic distribution and the temporal fluctuation of renewable energy resources represent challenges towards a sustainable energy transition. Moreover, the energy economy is relying on the material use of carbonaceous materials such as fuels, plastics, solvents or intermediates for the chemical industry, predominantly produced from fossil resources. In this regard, the Power-to-X (PtX) concept allows the use of renewable electricity in sectors that cannot be directly electrified by synthesizing quasi carbon-neutral fuels and chemicals from captured CO₂ and green hydrogen. Furthermore, the high energy density of liquid energy carriers allows a global transport and distribution of sustainable energy as well as a long-term and large-scale energy storage. This also

enables the defossilization of energy-intensive world regions with low renewable energy potential [1]. Studies estimate that by 2050, the European energy market alone will need between 550 to 1800 TWh of hydrogen and PtX products annually from which the major part is imported from areas with high renewable energy potential [2]. In the PtX context, dimethyl ether (DME) is a promising vector and energy carrier with diverse possible applications in different sectors. DME has a nominal hydrogen storage capacity of 26.1 wt-% [3], high gravimetric and volumetric energy density and is environmentally benign. This qualifies DME as a very attractive H₂ carrier for the global envisaged sustainable energy trade. Due to its relatively low vapor pressure of 0.6 MPa at 25 °C [4], DME is easily liquefied and a promising substitute or blending agent for LPG. Globally, almost 90 % of the current annual production of 5 Mt DME is used for LPG blending, predominantly in China [5]. In order to achieve a defossilization of the LPG sector only, the production capacity of renewable DME is projected to exceed 40 Mtpa by 2050 [6]. The high Cetane number and soot-free combustion qualify DME as a clean replacement for diesel fuel. Furthermore, DME is used as a propellant,

* Corresponding author.

E-mail address: ouda.salem@ise.fraunhofer.de (O. Salem).

<https://doi.org/10.1016/j.cej.2022.140525>

Received 14 September 2022; Received in revised form 17 November 2022; Accepted 19 November 2022

Available online 25 November 2022

1385-8947/© 2022 The Authors. Published by Elsevier B.V. This is an open access article under the CC BY license (<http://creativecommons.org/licenses/by/4.0/>).

Nomenclature

<i>A</i>	cross sectional area of the reactor [m ²]	<i>n_{H+}</i>	amount of acid sites [mol]
<i>Ads</i>	adsorption	\dot{N}	moleflow [mol s ⁻¹]
A36	Amberlyst 36	<i>N_{Data}</i>	Number of datapoints [-]
<i>c</i>	concentration [mol m ⁻³]	<i>p</i>	sampling port number
CAT400	Treverlyst CAT 400	\bar{p}	mean sampling port number
<i>d_{cat}</i>	Diameter of catalyst sphere [m]	<i>PtX</i>	Power-to-X
<i>D_i</i>	Molecular diffusion coefficient [m ² s ⁻¹]	<i>Q</i>	acid capacity [g mol ⁻¹]
<i>D_{eff}</i>	Effective diffusion coefficient [m ² s ⁻¹]	<i>r</i>	reaction rate [mol kg _{catalyst} ⁻¹ s ⁻¹]
<i>Des</i>	desorption	<i>R</i>	Universal gas constant [J K ⁻¹ mol ⁻¹]
<i>DME</i>	Dimethyl ether	<i>RLS</i>	rate-determining step
<i>E_A</i>	activation energy [J mol ⁻¹]	<i>SR</i>	surface reaction
<i>ER</i>	Eley-Rideal	<i>T</i>	Temperature [K]
<i>FT-IR</i>	Fourier-transform infrared spectroscopy	<i>TOS</i>	time on stream
<i>GC</i>	Gaschromatograph	<i>V</i>	volume [m ³]
ΔH_R^0	standard enthalpy of reaction [J mol ⁻¹]	<i>w</i>	weighting factor
<i>i</i>	subscript referring to component <i>i</i>	<i>WHSV</i>	weight hourly space velocity
<i>IER</i>	Ion exchange resin	<i>WSSRE</i>	weighted squared sum of relative errors
<i>k</i>	rate constant [mol kg _{catalyst} ⁻¹ s ⁻¹]	<i>x</i>	axial coordinate [m]
<i>k₀</i>	pre-exponential factor [mol kg _{catalyst} ⁻¹ s ⁻¹]	<i>X</i>	Conversion [-]
<i>K_{ads}</i>	ratio of adsorption constants	<i>y_i</i>	mole fraction of component <i>i</i> [-]
<i>K_{eq}</i>	equilibrium constant [-]	<i>Greek letters:</i>	
<i>K_i</i>	Adsorption constant of component <i>i</i>	α	Freundlich exponent
<i>L_C</i>	Characteristic length of catalyst particle [m]	η_w	water inhibition term
ΔL_{bed}	catalyst bed shift	ν	kinematic viscosity [m ² s ⁻¹]
<i>LH</i>	Langmuir-Hinshelwood	ρ	density [kg m ⁻³]
<i>m</i>	mass [kg]	θ_i	coverage of active sites with component <i>i</i> [-]
<i>MeOH</i>	Methanol	ψ	Weisz-Prater parameter [-]

refrigerant and solvent [5,7].

The conventional production process, also referred to as indirect route, is characterized by a gas phase reactor, two consecutive distillation columns for purification and the recycle of unreacted methanol (MeOH). Hereby, the purification and the evaporation of the MeOH feed are responsible for a high energy demand of the process. Furthermore, the two-step distillation and recycle process presents a large and complex plant configuration. An emerging alternative is the so-called direct route, where MeOH and DME synthesis occur in one reactor. While this leads to an increased equilibrium conversion compared to conventional MeOH synthesis, the separation of the unreacted syngas is significantly hampered due to the presence of DME, leading to a cumbersome and energy-intensive downstream process [8,9]. In the case of a CO₂-rich synthesis gas, the direct synthesis route becomes less favorable due to a lower equilibrium enhancement of the MeOH synthesis reaction and a complex downstream processing.

Locations with a high abundance of cheap renewable energy are often accompanied by insufficient infrastructure, limited construction area and high operation and maintenance costs [10]. PtX processes in such environments are thus required to exhibit low maintenance efforts, low area footprint and a low utility demand. Thus, highly integrated and simple processes with high energy efficiencies are desired. In this regard, both the direct route and the conventional indirect route have their drawbacks due to their large number of unit operations and high demand for external heat. Compared to these two DME production routes, a promising process intensification strategy is DME synthesis via reactive distillation, where the in-situ product removal allows a full conversion of the MeOH feedstock alongside the purification of the product DME and the by-product water [9]. This process alternative leads to a reduced number of unit operations and reduced maintenance efforts. Moreover, the reactive distillation concept allows the integration of the crude MeOH (a mixture of MeOH and water) distillation column into the reactive distillation column, since water is the by-product of both MeOH

and DME synthesis. Consequently, the exothermic heat of the MeOH process conventionally used for the crude MeOH distillation, can be integrated into a reactive distillation process based on the water containing crude MeOH as a feedstock [10]. Contrary to the conventional gas-phase synthesis at high temperature, the reactive distillation approach switches the reaction to the liquid phase, exploiting the benefits of the high relative volatility of DME in comparison to MeOH and water.

Despite the advantages of reactive distillation and the first operating commercial reactive distillation plant with a production capacity of ca. 10 kt_{DME}/a [11], research regarding the reaction kinetics of MeOH dehydration in the liquid phase is still limited to the use of the ion exchange resin (IER) Amberlyst® 35 with the reported kinetic models varying significantly among different scientific publications. Table 1 summarizes the current public literature on the reaction kinetics of DME synthesis in liquid phase. Besides the limited temperature range examined, the water content in the feed is limited to a molar fraction of 0.13 and 0.2 respectively. This, however, is insufficient for the description of reaction kinetics in the reactive distillation process, where water molar fractions up to $y_{H_2O} = 0.4$ are present in the reactive section of the column [12]. Additionally, most of the kinetic investigations in literature were carried out in batch reactors at vapor-liquid equilibrium, thus distorting the kinetic measurements due to the partial evaporation of the highly volatile DME from the liquid reaction phase.

In this work, the reaction kinetics of MeOH dehydration in the liquid phase are investigated experimentally over the wide temperature and feed composition range relevant for reactive distillation. Emphasis is put on reaction kinetics under a high water concentration, considering the application of crude MeOH in a reactive distillation process. Furthermore, kinetic models are derived for two catalysts, thus laying the foundation for a realistic design of DME reactive distillation processes towards industrial realization.

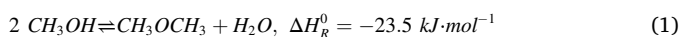
Table 1

Experimental parameter ranges and kinetic models of liquid phase MeOH dehydration to DME found in literature [13–15] compared to this work.

Author	Catalyst	Reactor	Phase	Temperature [°C]	$Y_{H_2O, Feed}$ [-]	Pressure [MPa]	Kinetic model
An et al. [13]	Amberlyst 35	Batch	Liquid-vapor	70–130	0–0.13	0.82	Eley-Rideal
Lei et al. [14]	Unspecified IER	Fixed-bed	Liquid	118–150	0–0.2	2.0	Eley-Rideal + Power law
Hosseininejad et al. [15]	Amberlyst 35	Batch	Liquid-vapor	110–135	0–0.13	0.9	Langmuir-Hinshelwood
This work	Amberlyst 36, Treverlyst CAT 400	Fixed-bed	Liquid	110–150 140–180	0–0.5	4.0 7.0	Langmuir-Hinshelwood with water inhibition term

2. Physico-chemical system characteristics

In the conventional production process, purified MeOH is evaporated and pre-heated for the equilibrium limited gas-phase dehydration of MeOH at 220–360 °C and 1–20 bar absolute pressure, according to the following equation [9]:



Following the reaction, the product mixture is purified by a two-step distillation process and unreacted MeOH is recycled to the reactor. Contrary to that, in a reactive distillation process, the reaction occurs in a vapor–liquid equilibrium between the involved components MeOH, DME and water. The physico-chemical system is hereby characterized by MeOH as a middle boiler, DME as the light boiler and water as the heavy boiler. In order to remove the produced DME and water from the reaction equilibrium in-situ, a temperature and pressure window in proximity to the MeOH boiling point curve has to be selected. Consequently, the process concept of reactive distillation dictates a narrow operating window at significantly lower reaction temperatures compared to the conventional process as illustrated by Fig. 1.

3. Material and methods

In this chapter the experimental methods including the chemicals as well as catalysts used in this study are presented. As two different experimental setups were utilized for catalyst screening and kinetic

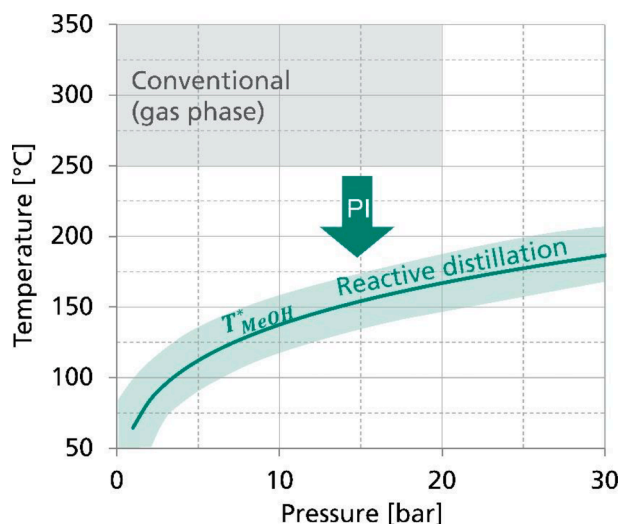


Fig. 1. Boiling point curve of MeOH and resulting operating window of a process-intensified (PI) reactive distillation process for DME synthesis compared to the operating conditions of the conventional gas phase reaction.

measurements, they are described in separate sections. Finally, the simulation model as well as the parameter fitting methodology for the kinetic approaches will be introduced.

3.1. Chemicals

The chemicals used as feedstock and for GC calibration were synthesis grade MeOH (99.9 vol-%, Chemsolute®), Dimethylether 3.0 (99.9 %, Linde plc) and deionized water obtained from the in-house system. Nitrogen of grade 5.0 was used for dilution purposes.

3.2. Ion exchange resins

Two types of cationic IER were used: Macroporous oversulfonated IER and macroporous chlorinated IER with significantly higher temperature stability, but lower acid capacity (see Table 2). Amberlyst 36 (A36) was obtained from Merck KGaA, Treverlyst IER were supplied by CHEMRA GmbH and the Purolite IER were supplied by Purolite GmbH. Each IER was dried in a vacuum oven (50 mbar, 100 °C, 24 h) and weighed in dry state as distinct reference. After drying, the resin was submerged in MeOH for at least 2 h to achieve the fully swollen state.

3.3. Zeolites

The four zeolites used within this study and shown in Table 3 exhibit different Si/Al-ratios and frameworks and were supplied by Clariant AG. Zeolites provided in powder form were pelletized first, to obtain a starting material comparable to the zeolites provided in extruded form. Finally, all zeolites were crushed and sieved to a particle size between 300 µm and 700 µm.

3.4. Perfluorsulfonic acids

Two variants of solid perfluorsulfonic acids, namely Nafion NR 40 (DuPont de Nemours) and Aquivion PW79S (Solvay GmbH) were used.

Table 2
IER used in this study with their corresponding technical data.

IER	Acid capacity [meq/g]	Max. temperature [°C]	Resin type
Amberlyst 36	5.4	150	Oversulfonated
Treverlyst CAT 360	5.4	150	Oversulfonated
Treverlyst CAT 400	2.7	190	Sulfonated and chlorinated
Purolite CT 275	5.2	130	Oversulfonated
Purolite CT 169	4.7	130	Oversulfonated
Purolite CT 482	2.7	190	Sulfonated and chlorinated

Table 3

Zeolites used in this study with their corresponding technical data.

Zeolite	Si/Al	Zeolite framework	Original form
H-CZB 30	30	BEA	Powder
H-CZB 150	150	BEA	Extruded
H-CZP 90	90	MFI	Extruded
H-CZM 40	40	MOR	Extruded

This catalyst class is characterized by a lower acid capacity but a higher acid strength and higher temperature stability compared to IER as summarized in Table 4 [16].

3.5. Experimental setup and procedure

3.5.1. Catalyst screening

The catalyst screening was conducted in a parallelized batch autoclave system manufactured by H.E.L. Group, consisting of 8 parallel stirred batch autoclaves with a reactor volume of 60 ml each. These autoclaves were filled with 35 ml of MeOH and 1 g of each respective catalyst. The reactors were pressurized with nitrogen to 30 bar to prevent the MeOH feed from evaporating. Mixing throughout the experiments was ensured by a mechanical stirrer with a variable rotational speed up to 1000 rpm. During the heating period kept below 10 min for all experiments as well as the screening experiments, the stirrer was operated at a constant speed of 500 rpm. It was validated that the stirrer speed has no influence on the conversion pursuing a mass transfer limitation test at different stirring speeds. Each autoclave could be heated individually by a thermal oil basin and an electric copper heating jacket. Reaction temperature was monitored and controlled by a thermocouple placed in direct contact with the reaction mixture. All catalysts were screened at a temperature of 150 °C, those with higher temperature stability were also tested at 170 °C. After a reaction time of 2 h the reaction was quenched, and a sample was withdrawn via an immersion pipe equipped with a sinter filter (10 µm pore diameter) to prevent unintended catalyst withdrawal. Analysis of the sample composition was done with an Agilent 6890 gas chromatograph (GC) equipped with HP-Plot Q column (30 m column length, 0.53 mm internal diameter, 40 µm film thickness) and a thermal conductivity detector. The oven temperature was constant at 100 °C, the detector temperature was at 220 °C. Due to the high vapor pressure of the liquid mixture, a liquid injection into the GC was not feasible, and the sample needed to be completely evaporated prior to analysis in the GC. For this purpose, samples were withdrawn in a pressurized sample apparatus and subsequently injected into an evaporation system consisting of a heated pressure vessel before being injected to the GC. Each sample was analyzed three times to minimize measurement errors. Fig. 2 shows a simplified illustration of the complete screening setup.

3.5.2. Kinetic measurements

A schematic flow diagram of the used Kinetic Investigations and Screening Setup KISS developed at Fraunhofer ISE [17] is illustrated in Fig. 3. Mixtures of MeOH and H₂O were added in a feed tank with a volume of 2.5 L and dosed to the reactor by coupling an HPLC-pump and a Coriolis mass flow controller. The reaction was performed in a profile reactor consisting of a stainless-steel tube with a length of 450 mm and 8 mm internal diameter equipped with fiber optical temperature measurement system. The reactor was jacketed in a solid aluminum shell

Table 4

Perfluorosulfonic acids used in this study with their corresponding technical data.

IER	Acid capacity	Max. temperature	Chlorinated?
	[Meq/g]	[°C]	
Nafion NR40	1.0	200	No
Aquivion PW79S	1.23–1.3	240	No

equipped with four heating cartridges to allow uniform heating and dissipation of exothermic reaction heat. All experiments showed a nearly ideally isothermal temperature profile with less than 0.5 K deviation from the mean temperature throughout the reactor.

The reactor was filled with a catalyst bed of commercial IER, held in place by two inert beds of SiO₂ (600–710 µm, Sigmund Lindner GmbH). To achieve a homogenous catalyst bed without cavities, the reactor was filled with the fully swollen resin while rinsing with MeOH. Centered inside the reactor tube is a stainless-steel capillary of 0.8 mm external diameter equipped with a glass fiber for fiber optic measurement of the axial temperature profile. Due to axial variation of the refractive index, waveguide geometry distortions or local defects light guided through this glass fiber is backscattered. Applying discrete Fourier transformation the resulting signal can be translated to a high-resolution temperature profile [18,19]. A spatial resolution of 2.6 mm and a temporal resolution of 5 s was selected for the measurement campaign in this study. The fiber optic measurement system was calibrated by heating the reactor isothermally to a reference temperature measured with a Pt-100 temperature sensor. The resulting calibration curve was then fitted with a third order polynomial (see Supplementary information).

For the measurement of the composition profile in the reactor, sampling ports are axially distributed with a spacing of 68 mm and connected to a multiposition valve, transferring the selected stream to a back-pressure regulator heated by an electric heating band. Here, the liquid stream was completely evaporated and consequently forwarded to an MKS Multigas™ 2030 on-line FT-IR spectrometer with an optical path length of 35 cm for analysis. The reactants MeOH, DME, H₂O and potential side products such as CH₄ and Formaldehyde were calibrated. The calibration method was provided by ASG Analytik-Service AG. The reaction product was diluted with nitrogen to avoid condensation of the evaporated sample and to improve spectral quality by avoiding excessive absorption of the infrared beam. The reactor outlet mass flow was controlled by a second Coriolis mass flow controller, thus allowing a precise adjustment of the distribution between reactor outlet stream and sampling port stream.

The experimental conditions of the measured data points are summarized in Table 5 and were chosen to allow a precise modelling of the apparent kinetics of commercial sized IER particles over the relevant operating range. Each combination of the listed parameters was performed experimentally. A36 experiments were not performed at the combination of $y_{\text{H}_2\text{O}, \text{Feed}} = 0.5$ at $T_{\text{R}} = 110$ °C and $T_{\text{R}} = 120$ °C as well as the combination of $T_{\text{R}} = 110$ °C at $y_{\text{H}_2\text{O}, \text{Feed}} = 0.3$, due to the negligibly low MeOH conversion at those conditions. The kinetic measurements for A36 were performed at a pressure of 40 bar, while for Treverlyst CAT 400, the higher operating temperature necessitated a higher operating pressure of 70 bar to guarantee a liquid phase reaction without partial evaporation of the mixture. Pressure variation was verified to have no influence on the conversion of the reaction. Mole fractions of MeOH and H₂O in the feed were varied to examine the water-influence on reaction kinetics independent of the DME content. High water contents up to $y_{\text{H}_2\text{O}} = 0.5$ were examined for two reasons:

1. In the composition profile of DME reactive distillation processes, water fractions up to $y_{\text{H}_2\text{O}} = 0.4$ are present [12].
2. The crude MeOH in CO₂-based MeOH synthesis contains a water content up to $y_{\text{H}_2\text{O}} = 0.5$ [20].

Due to the profile reactor concept, every reactor profile comprises 6 measurement points of different weight hourly space velocity (WHSV). To ensure the absence of external mass transfer limitations at all studied operation points, the reactor was operated at different sampling ports and different feed flows to achieve a constant WHSV under varying flow velocities. At the maximum operating temperature and no water in the feed it was verified that the flow velocity had no influence on MeOH conversion and thus external mass transfer limitations are negligible in

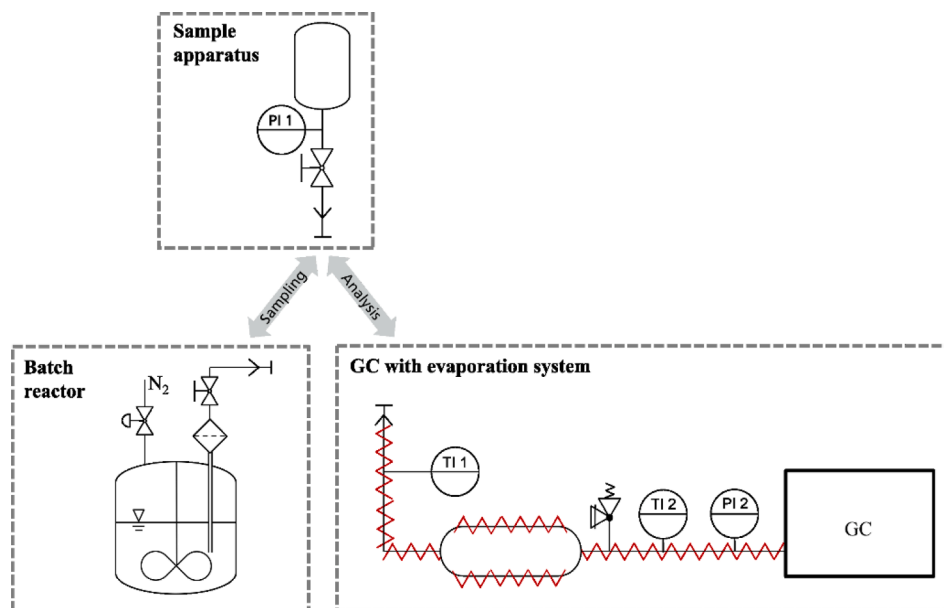


Fig. 2. Process setup for the catalyst screening consisting of the batch reactor system, the sample apparatus and the evaporation system coupled with the GC.

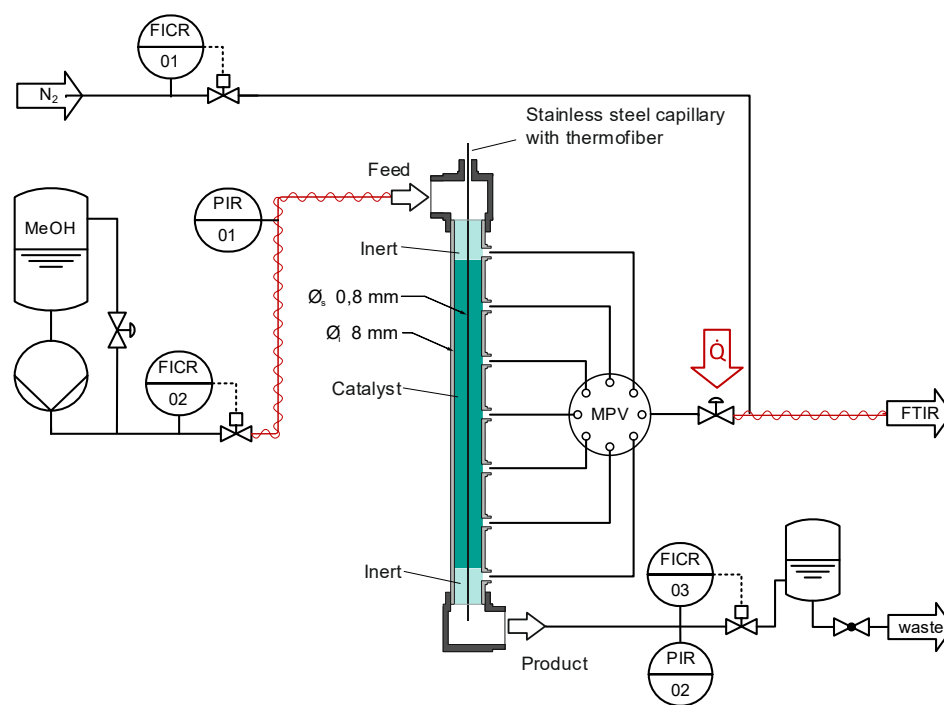


Fig. 3. Process flow diagram of the kinetic test stand with liquid feed dosing, profile reactor and the corresponding FT-IR analytics.

Table 5

Experimental operating parameters applied during the kinetic measurements.

Variable	Unit	Amberlyst 36	Treverlyst CAT 400
WHSV	1/h	16–270	16–220
Temperature	$^{\circ}C$	110; 120; 130; 140; 150	140; 150; 160; 170; 180
Pressure	bar	40	70
$Y_{H_2O, Feed}$	mol/mol	0; 0.02; 0.1; 0.3; 0.5	0; 0.02; 0.1; 0.3; 0.5
Catalyst mass	g	7.38	7.48

the investigated range (see [Supplementary information](#)). Furthermore, the influence of internal mass transfer was estimated using the Weisz-Prater parameter [21,22] and it was found that internal mass transfer

limitations can be neglected (see [Supplementary information](#)). Consequently, the measured kinetics is intrinsic. Since the reaction rate decreases with lower temperature and higher water content in the feed, it

is guaranteed that reaction kinetics is the limiting step at all operating points considered. The catalyst bed height when filled was 410 mm for both IER, due to differences in bed density between the two IER, the total catalyst mass varied slightly. For the measurement of a concentration profile, the sampling ports were selected against the flow direction. Due to the on-line analytics, a steady state operation could be observed in the software of the FTIR. Once steady state was achieved, the reactor was operated constantly for another minute in which FTIR measurements were averaged. Considering the measurement frequency of 1 Hz, this corresponds to a 60-fold replicated measurement.

3.5.3. Acid capacity determination

Determination of the IER's acid capacity was performed by titration. For this purpose, dried catalyst was put in an excess of a standard NaOH solution ($c_{\text{NaOH},0} = 0.1$ mol/L) overnight to neutralise all acid groups. Subsequently, the supernatant NaOH solution was titrated with sulfuric acid ($c_{\text{H}_2\text{SO}_4} = 0.1$ mol/L) to determine the base concentration of the NaOH solution in equilibrium $c_{\text{NaOH},\text{eq}}$. By comparing the base concentration with the original standard NaOH solution concentration, the acid capacity Q_{IER} of the catalyst can be calculated according to Eq. (2):

$$Q_{\text{IER}} = \frac{n_{\text{H}^+}}{m_{\text{IER}}} = \frac{V_{\text{sample}} \cdot (c_{\text{NaOH},0} - c_{\text{NaOH},\text{eq}})}{m_{\text{IER}}} \quad (2)$$

3.6. Reactor modelling

The reactor model was based on a one-dimensional steady state reactor model assuming ideal plug flow behavior. At the studied conditions, the dimensionless Bodenstein number at the experimental conditions applied in the kinetic study was calculated to be $Bo = 476$ based on the dimensionless Péclet number, Schmidt number and Reynolds number as described in Kraume et al. [23]. Consequently the neglect of axial dispersion is justified [23]. The basis of the model is the material balance over the length of the reactor, as described in Eq. (3). Due to the effective dissipation of exothermic heat, the profile reactor was nearly ideally isothermal. To account for the minor temperature changes along the reactor bed, the fiber optic measured temperature profile of each experimental run was implemented in the simulation model to simulate every increment of the reactor with the precise measured temperature. Consequently, no energy balance was required in the reactor simulation. An impulse balance was omitted since the pressure drop in all the experiments was measured below 100 mbar.

$$\frac{d\dot{N}_i}{dx} = r_i \cdot \rho_{\text{cat, bulk}} \cdot A_0 \quad (3)$$

Table 6

Basic rate equations for LH and ER mechanism depending on the RDS.

RDS	Langmuir-Hinshelwood	Eley-Rideal
Adsorption of MeOH	$r_{\text{DME}} = \frac{k \cdot \left(y_{\text{MeOH}} - \frac{y_{\text{DME}} \cdot y_{\text{H}_2\text{O}}}{K_{\text{eq}}} \right)^{0.5}}{\left(\frac{y_{\text{DME}} \cdot y_{\text{H}_2\text{O}}}{K_{\text{eq}}} \right)^{0.5} + K_{\text{ads}} \cdot y_{\text{H}_2\text{O}}} \quad (5)$	$r_{\text{DME}} = \frac{k \cdot \left(y_{\text{MeOH}} - \frac{y_{\text{DME}} \cdot y_{\text{H}_2\text{O}}}{K_{\text{eq}} \cdot y_{\text{MeOH}}} \right)}{\left(\frac{y_{\text{DME}} \cdot y_{\text{H}_2\text{O}}}{K_{\text{eq}} \cdot y_{\text{MeOH}}} \right) + K_{\text{ads}} \cdot y_{\text{H}_2\text{O}}} \quad (6)$
Surface-reaction	$r_{\text{DME}} = \frac{k \cdot \left(y_{\text{MeOH}}^2 - \frac{y_{\text{DME}} \cdot y_{\text{H}_2\text{O}}}{K_{\text{eq}}} \right)}{\left(y_{\text{MeOH}} + K_{\text{ads}} \cdot y_{\text{H}_2\text{O}} \right)^2} \quad (7)$	$r_{\text{DME}} = \frac{k \cdot \left(y_{\text{MeOH}}^2 - \frac{y_{\text{DME}} \cdot y_{\text{H}_2\text{O}}}{K_{\text{eq}}} \right)}{y_{\text{MeOH}} + K_{\text{ads}} \cdot y_{\text{H}_2\text{O}}} \quad (8)$
Desorption of H ₂ O	$r_{\text{DME}} = \frac{k \cdot \left(K_{\text{eq}} \frac{y_{\text{MeOH}}^2}{y_{\text{DME}}} - y_{\text{H}_2\text{O}} \right)}{K_{\text{ads}} \cdot y_{\text{MeOH}} + K_{\text{eq}} \frac{y_{\text{MeOH}}^2}{y_{\text{DME}}}} \quad (9)$	$r_{\text{DME}} = \frac{\frac{k_{\text{H}_2\text{O}}}{K_{\text{H}_2\text{O}}} \cdot \left(K_{\text{eq}} \frac{y_{\text{MeOH}}^2}{y_{\text{DME}}} - y_{\text{H}_2\text{O}} \right)}{K_{\text{ads}} \cdot y_{\text{MeOH}} + K_{\text{eq}} \frac{y_{\text{MeOH}}^2}{y_{\text{DME}}}} \quad (10)$

The thermochemical properties and transport properties of the liquid mixture required for the reactor modeling and the calculation of the Bodenstein number, were calculated based on the correlations summarized in the [supplementary material \[24–28\]](#).

3.7. Kinetic modelling

The examined kinetic models were derived from the Hougen-Watson approach. Hereby a distinction was made between the Langmuir-Hinshelwood (LH) and the Eley-Rideal (ER) mechanism: While the LH mechanism assumes that two MeOH molecules adsorb on two adjacent active sites Z of the catalyst, the Eley-Rideal mechanism assumes the adsorption of only one MeOH molecule on an active site, which then reacts with another MeOH molecule from the bulk phase. After the surface reaction, the reaction products DME and water desorb into the liquid bulk phase.

	Langmuir-Hinshelwood	Eley-Rideal
Adsorption:	$\text{MeOH} + \text{Z} \rightleftharpoons \text{MeOH}^* \text{Z}$	$\text{MeOH} + \text{Z} \rightleftharpoons \text{MeOH}^* \text{Z}$
Surface reaction:	$2\text{MeOH}^* \text{Z} \rightleftharpoons \text{DME}^* \text{Z} + \text{H}_2\text{O}^* \text{Z}$	$\text{MeOH} + \text{MeOH}^* \text{Z} \rightleftharpoons \text{DME}^* \text{Z} + \text{H}_2\text{O}^* \text{Z}$
Desorption:	$\text{DME}^* \text{Z} \rightleftharpoons \text{DME} + \text{ZH}_2\text{O}^* \text{Z} \rightleftharpoons \text{H}_2\text{O} + \text{Z}$	$\text{DME}^* \text{Z} \rightleftharpoons \text{DME} + \text{ZH}_2\text{O}^* \rightleftharpoons \text{H}_2\text{O} + \text{Z}$

Depending on the rate-determining step (RDS) being either the MeOH adsorption, the surface reaction, or the product desorption, three kinetic expressions can be derived for each mechanism respectively. All the kinetic expressions can be described by the general mathematical Hougen-Watson expression, as described by Eq. (4) [29].

$$\Gamma_{\text{DME}} = \frac{\text{kinetic term} \cdot \text{driving force}}{(\text{adsorption term})^n} \quad (4)$$

IER exhibit a significant swelling behavior, leading to a significant increase in volume when subjected to a polar medium. Since more polar components have a higher affinity towards the electronegative sulfonic groups in the resin, swelling is a highly selective process, leading to a preferred adsorption of the more polar components over the less polar components [30–32]. Due to the low polarity of DME compared to the strong polarity of MeOH and water, DME has a significantly lower affinity towards the electronegative sulfonic groups in the resin and consequently, the adsorption term of DME was neglected in the reaction network. Furthermore, the term $\frac{1}{K_{\text{MeOH}}}$ was neglected because it was supposed to be very small compared to the other components of the denominator and consequently the adsorption term in the kinetic expression can be simplified, as shown in the rate equations summarized in [Table 6](#).

With

$$K_{eq} = \exp\left(1.743 + \frac{887.9}{T}\right) \text{ Own correlation based on the Gibbs free energy of reaction according to Aspen Plus.} \quad (11)$$

$$K_{Ads} = \frac{K_{H_2O}}{K_{MeOH}} = \exp\left(K_{Ads,1} - \frac{K_{Ads,2}}{T}\right) \quad (12)$$

$$k = k_0 \cdot \exp\left(\frac{-E_A}{R T}\right) \quad (13)$$

To account for the strong inhibitory effect of water, a dedicated inhibition term was introduced. This term incorporates the fact, that water has a very high affinity towards the active sites, thus blocking some of the acid sites which consequently cannot participate in the reaction. The fraction of acid sites blocked by water θ_{H_2O} can be expressed either by the Langmuir or the Freundlich adsorption isotherm as shown in Table 7 [33]. Consequently, the inhibition term is defined as $\eta_w = 1 - \theta_{H_2O}$. By adding the water inhibition term, the kinetic rate equation was extended by the sorption coefficient K_W expressed by the two additional fitting parameters K_{W1} and K_{W2} and in case of the Freundlich-based approach by the Freundlich exponent α expressed by the additional fitting parameter K_α .

$$K_W = \exp\left(K_{W1} - \frac{K_{W2}}{T}\right) \quad (14)$$

$$\alpha = K_\alpha / T \quad (15)$$

The resulting overall reaction rate expression is obtained by multiplying the conventional ER and LH rate expressions with the water inhibition term. Hereby the amount of acid sites involved in the reaction

Table 7
Fraction of acid sites blocked by water θ_{H_2O} and resulting water inhibition term η_w according to Langmuir [33] and Freundlich isotherm [34].

Adsorption isotherm	θ_{H_2O}	Water inhibition term: $1 - \theta_{H_2O}$
Langmuir, one water molecule blocks one active site	$\theta_{H_2O} = \frac{K_W \cdot y_{H_2O}}{1 + K_W \cdot y_{H_2O}}$ (16)	$\eta_w = \frac{1}{1 + K_W \cdot y_{H_2O}}$ (17)
Langmuir, one water molecule blocks two active sites	$\theta_{H_2O} = \frac{K_W \cdot \sqrt{y_{H_2O}}}{1 + K_W \cdot \sqrt{y_{H_2O}}}$ (18)	$\eta_w = \frac{1}{1 + K_W \cdot \sqrt{y_{H_2O}}}$ (19)
Freundlich	$\theta_{H_2O} = K_W \cdot y_{H_2O}^\alpha$ (20)	$\eta_w = 1 - K_W \cdot y_{H_2O}^\alpha$ (21)

Table 8
Extended rate equations for LH and ER mechanism with added water inhibition term. RDS: surface reaction.

Water correction term	Langmuir-Hinshelwood	Eley-Rideal
Langmuir, one water molecule blocks one active site	$r_{DME} = \frac{k \cdot \left(y_{MeOH}^2 - \frac{y_{DME} \cdot y_{H_2O}}{K_{eq}}\right)}{\left(y_{MeOH} + K_{ads} \cdot y_{H_2O}\right)^2 \cdot \left(1 + K_W \cdot y_{H_2O}\right)^2}$ (22)	$r_{DME} = \frac{k \cdot \left(y_{MeOH}^2 - \frac{y_{DME} \cdot y_{H_2O}}{K_{eq}}\right)}{y_{MeOH} + K_{ads} \cdot y_{H_2O}} \cdot \frac{1}{1 + K_W \cdot y_{H_2O}}$ (23)
Langmuir, one water molecule blocks two active sites	$r_{DME} = \frac{k \cdot \left(y_{MeOH}^2 - \frac{y_{DME} \cdot y_{H_2O}}{K_{eq}}\right)}{\left(y_{MeOH} + K_{ads} \cdot y_{H_2O}\right)^2 \cdot \left(1 + K_W \cdot \sqrt{y_{H_2O}}\right)^2}$ (24)	$r_{DME} = \frac{k \cdot \left(y_{MeOH}^2 - \frac{y_{DME} \cdot y_{H_2O}}{K_{eq}}\right)}{y_{MeOH} + K_{ads} \cdot y_{H_2O}} \cdot \frac{1}{1 + K_W \cdot \sqrt{y_{H_2O}}}$ (25)
Freundlich	$r_{DME} = \frac{k \cdot \left(y_{MeOH}^2 - \frac{y_{DME} \cdot y_{H_2O}}{K_{eq}}\right)}{\left(y_{MeOH} + K_{ads} \cdot y_{H_2O}\right)^2} \cdot \left(1 - K_W \cdot y_{H_2O}^\alpha\right)$ (26)	$r_{DME} = \frac{k \cdot \left(y_{MeOH}^2 - \frac{y_{DME} \cdot y_{H_2O}}{K_{eq}}\right)}{y_{MeOH} + K_{ads} \cdot y_{H_2O}} \cdot \left(1 - K_W \cdot y_{H_2O}^\alpha\right)$ (27)

mechanism (ER: 1, LH: 2) needs to be considered and consequently the

water inhibition term is squared for the LH-models [35].

The resulting rate expressions of the extended kinetic models are summarized in Table 8.

In total, 12 different rate equations were derived, 6 basic ER and LH rate equations (Eqs. (5)–(10)), and 6 extended ER and LH rate equations (Eqs. (22)–(27)).

3.8. Kinetic fitting and validation

The reactor model (section 3.2) was implemented in MATLAB® (version R2020a) and used to simulate all measured data points. Besides feed mass flow and composition, the measured temperature profiles obtained during the experiments were considered in the reactor simulation. An overview of the methodology is illustrated in Fig. 4.

The deviation between simulated and experimental reaction conversion was minimized in an optimization by varying the fitting parameters of the respective kinetic model. The objective function for the fitting was defined as the weighted sum of squared relative errors (WSSRE) of MeOH conversion X . Due to the equimolar reaction equation, the MeOH conversion can be calculated based on the molar fractions.

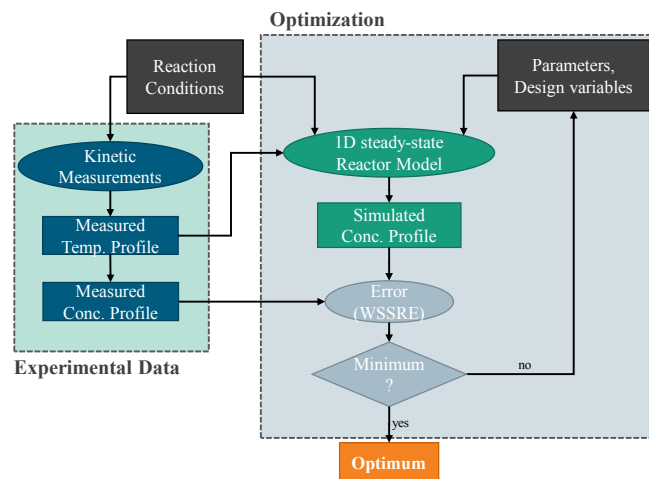


Fig. 4. Kinetic fitting methodology applied in this study.

$$WSSRE = \sum_{j=1}^{N_{data}} \left(\frac{X_{MeOH, Exp.i} - X_{MeOH, Sim.i}}{X_{MeOH, Exp.i}} \cdot 100 \cdot w_j \right)^2 \quad (28)$$

$$X_{MeOH} = \frac{\dot{N}_{MeOH,0} - \dot{N}_{MeOH}}{\dot{N}_{MeOH,0}} = \frac{y_{MeOH,0} - y_{MeOH}}{y_{MeOH,0}} \quad (29)$$

$$w_j = \frac{p_j}{\bar{p}} \quad (30)$$

The relative error was preferred to the absolute error to avoid a disproportionate weighting of operating points with high conversion. Due to a large variation in feed compositions and reaction temperatures, the conversion in the experiments varied significantly. Using the absolute error of the MeOH conversion would consequently lead to an underweighting of operating points with low temperature and/or low MeOH feed concentration. To account for the higher precision of measurements with increasing bed height (see [Supplementary information](#)) a weighting factor w_i was additionally considered, defined as the sampling port number p_j divided by the mean sampling port number \bar{p} . Experimental data obtained in the examination of external mass transport limitations was not used for the kinetic fitting to avoid an over-weight of experimental data with a feed of pure MeOH.

The minimization of the WSSRE was performed with a Nelder-Mead simplex algorithm [36] implemented by the `fminsearch` function in MATLAB®. To avoid local minima, the algorithm was started from 6 randomly distributed starting parameters and respectively called repeatedly until the result of two consecutive optimization runs was identical.

The function's residuals and jacobian matrix at the optimization solution were calculated using the Matlab® function `lsqnonlin`. Confidence intervals were obtained based on the Jacobian matrix and residuals with the MATLAB® function `nlparci`.

4. Results and discussion

4.1. Catalyst screening in batch reactor

Fig. 5 illustrates the MeOH conversion for all catalysts tested in the screening experiments. Both perfluorsulfonic acids Nafion and Aquivion proved to be unstable and are thus not included in the diagram. No side-products were detected for any examined catalyst. Macroporous

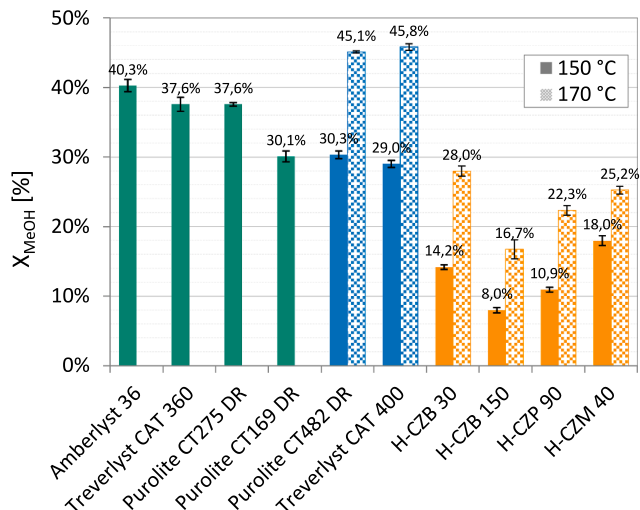


Fig. 5. MeOH conversion to DME in batch autoclaves using various catalysts at 150 °C (solid bar) and 170 °C (checked bar) respectively. Reaction parameters: 35 ml MeOH sample volume, 1 g catalyst, 30 bar initial reaction pressure, 2 h reaction time, 500 rpm stirrer speed. All tests were carried out using pure MeOH feed.

oversulfonated IER (green) exhibit the highest catalytic activity at 150 °C, with conversions between 30 % and 40 %. Amberlyst 36, CAT 360 and CT275 DR show a comparable conversion of more than 37 % while only 30.1 % were obtained with CT169 DR. This trend can partly be related to the acid capacity of the IER, which is slightly lower for CT169 DR compared to the other oversulfonated resins (compare [Table 2](#)). The chlorinated IER (blue) generally show lower MeOH conversions at 150 °C than the oversulfonated resins with the exception of CT169 DR which shows a similar conversion. Due to the higher temperature stability of the chlorinated resins however, higher conversions than with the oversulfonated resins can be achieved when the reaction temperature is increased to 170 °C. This result emphasizes the potential of high-temperature stable resins in the liquid phase MeOH dehydration and evokes the need for kinetic models of DME-synthesis using chlorinated IER to fully explore their potential.

Regarding the performance of zeolites, a correlation between the Si/Al-ratio and the catalytic activity can be drawn at 170 °C. At 150 °C the correlation can be drawn with the exception of H-CZB 30, which shows lower a conversion than expected. Lower Si/Al-ratios increase the acidity of the zeolite and consequently its activity. In the gas-phase DME synthesis, an optimal Si/Al ratio needs to be found in order to find a compromise between activity and selectivity [37]. In contrast, the liquid phase DME synthesis at mild conditions allows lower Si/Al ratios without compromising selectivity. However, regarding the absolute activity at the studied conditions, all the tested zeolites were outperformed by oversulfonated resins and chlorinated resins. Even the most active zeolite was found less active at 170 ° than the least active IER at 150 °C. Since no absolute maximum is indicated for the operating temperature of zeolites, conversions exceeding 45 % might be possible at temperatures above 170 °C. However, higher temperatures would require increased operational pressures in a reactive distillation process. Furthermore, at such conditions, the deactivation by Si dissolution from the zeolite needs to be critically evaluated as shown by Sun et al. [38].

Both perfluorsulfonic acids investigated in this study proved to be unstable under the reaction conditions applied. While the exposure of Nafion NR40 to MeOH at room temperature led to a strong swelling, the catalyst was completely dissolved under the reaction conditions. Aquivion PW79S showed a strong structural change from its crystalline state to a highly swollen state in MeOH at room temperature and a gel-type state after the reaction. The evaporation of the reaction product led to significant residues, indicating a partial dissolution of the Aquivion. The different behavior of both perfluorsulfonic acids can be explained by the shorter side chain of Aquivion compared to Nafion, leading to a stronger electrostatic attraction of the side chain and the polymer backbone. In summary, the perfluorsulfonic acids considered here were found inappropriate for the liquid phase DME synthesis and are thus not further considered.

4.2. Kinetic measurements in profile reactor

Overall, Amberlyst 36 as the most active oversulfonated resin and Treverlyst CAT 400 as the most active chlorinated resin were identified as the most promising catalysts among all considered catalysts and were thus selected for detailed kinetic measurements. In the profile reactor measurements, a significant shrinkage of the catalyst bed after the filling process could be detected by investigation of the axial temperature profile along the reactor. Due to the vertical alignment of the reactor, this shrinkage led to a reduced catalyst mass in the reactor part upstream of the first sampling port. The exact extend of the bed shrinkage could be quantified by the temperature jump based on the exothermic heat released in the section of the catalyst bed but not in the inert bed. Further information regarding these findings are provided in the [supplementary material](#). At all examined reaction conditions, no side-products could be detected confirming the analysis in the batch campaign.

Fig. 6 compares the MeOH conversion of both catalysts for all

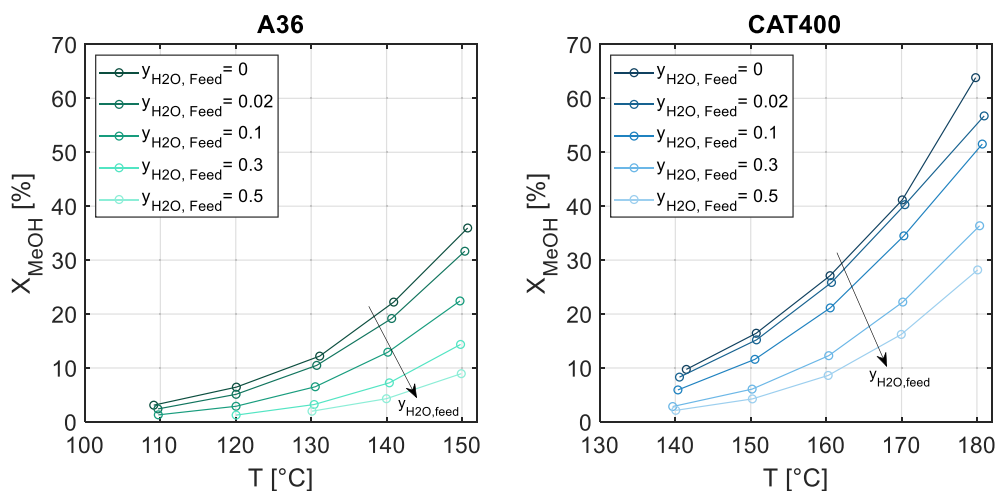


Fig. 6. MeOH conversion over reaction temperature obtained with A36 and CAT400 for various water fractions in the feed. Display of the last sampling port at WHSV = 16.2 h⁻¹ only.

reaction temperatures and feed water fractions. For simplification, only the conversion at the last sampling port is shown, corresponding to WHSV = 16.2 h⁻¹.

Each curve shows a characteristic exponential behavior as expected by the Arrhenius equation. Furthermore, the inhibiting effect of water is apparent when comparing the curves of different feed water fractions. Hereby it becomes obvious, that the water inhibition is nonlinear, with a feed water fraction of 10 % leading to a conversion reduction of 38 % for A36 (at 150 °C). When comparing both catalysts at the same operating temperature and water feed fraction, it can be noticed that the conversion of CAT400 is lower by a factor of approximately two. This lower activity can quantitatively be explained by the ratio of acid capacity $C_{A36} / C_{CAT400} = 5.4/2.7 = 2$. However, the lower activity of CAT400 is overcompensated by the higher maximum operating temperature. Only a temperature increase of 10–15 °C – depending on the feed water fraction – is required to achieve the same MeOH conversion. When comparing both catalysts at the maximum operating temperature, the MeOH conversion with CAT 400 is higher by a factor of 3 and 1.8 at feed water fractions of 0.5 and 0 respectively. These measurements clearly show that despite their lower acid capacity, chlorinated IER show great potential for the liquid phase MeOH dehydration.

During the measurement campaign, explicit benchmark conditions were applied immediately after the filling of the catalyst and repeatedly afterwards at different times during the measurement campaign. This

way, the conversion at a specific time could be related to the initial conversion with fresh catalyst to examine a potential decrease in catalyst activity during the measurement campaign. Furthermore, the acid capacity of the fresh and used catalysts were determined experimentally. Hereby, a noticeable decrease in conversion and acid capacity was observed for both catalysts. Details regarding this can be found in the [supplementary material](#). However, due to the limited number of data points and the limited operating time, it remains unclear whether the activity loss is just an initial behavior, or a continuous trend. Furthermore, it is uncertain whether the observed activity loss is reversible and can be regenerated by acid treatment [24]. Consequently, no definite statement can be made regarding the long-term stability of the catalysts examined in the kinetic study. Future work should focus on long-term experiments, examining the IER stability under various operating conditions.

4.3. Kinetic modelling

While all published literature on DME synthesis on IER assume a very fast educt adsorption and product desorption compared to the surface reaction, kinetic models with adsorption or desorption as RDS have not been examined yet. Fig. 7 shows the WSSRE of both fitted basic ER and LH models with the RDS being either the adsorption of MeOH (Ads), the surface reaction (SR) or the desorption of water (Des) for both catalysts examined in the kinetic study. Every model was fitted based on all measured datapoints listed in the [supplementary material](#). The graph clearly indicates that for both ER and LH, the model with the surface reaction as RDS represents the best fit regardless of the used catalyst. This result indicates that adsorption and desorption are in fact faster than the surface reaction. For this reason, in the following sections only the two models ER_{SR} and LH_{SR} are investigated further.

To compare ER_{SR} and LH_{SR} model in more detail, Fig. 8 shows the relative error of experimental data and simulation data depending on reaction temperature and water fraction of feed for A36 and CAT400. A positive relative error indicates a higher simulated than measured conversion.

The distribution of the relative error is comparable for both kinetic models, consequently both models are equally capable to describe the measured data. However, it becomes obvious that the error of both models depends significantly on the water fraction. While both models deliver a high precision at low water fractions, water fractions between 0.2 and 0.35 lead to a significant overestimation of the catalyst's activity. Furthermore, water fractions >0.4 lead to a strong underestimation of the reaction rate. This model inaccuracy is more pronounced

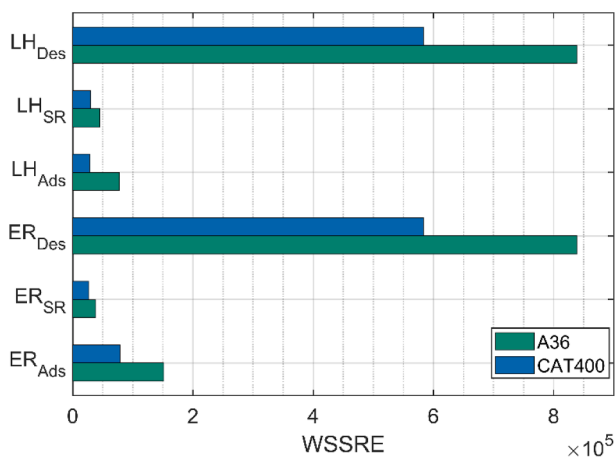


Fig. 7. WSSRE of fitted basic ER and LH models with the RDS being either adsorption, surface reaction or desorption for both catalysts examined in the kinetic study.

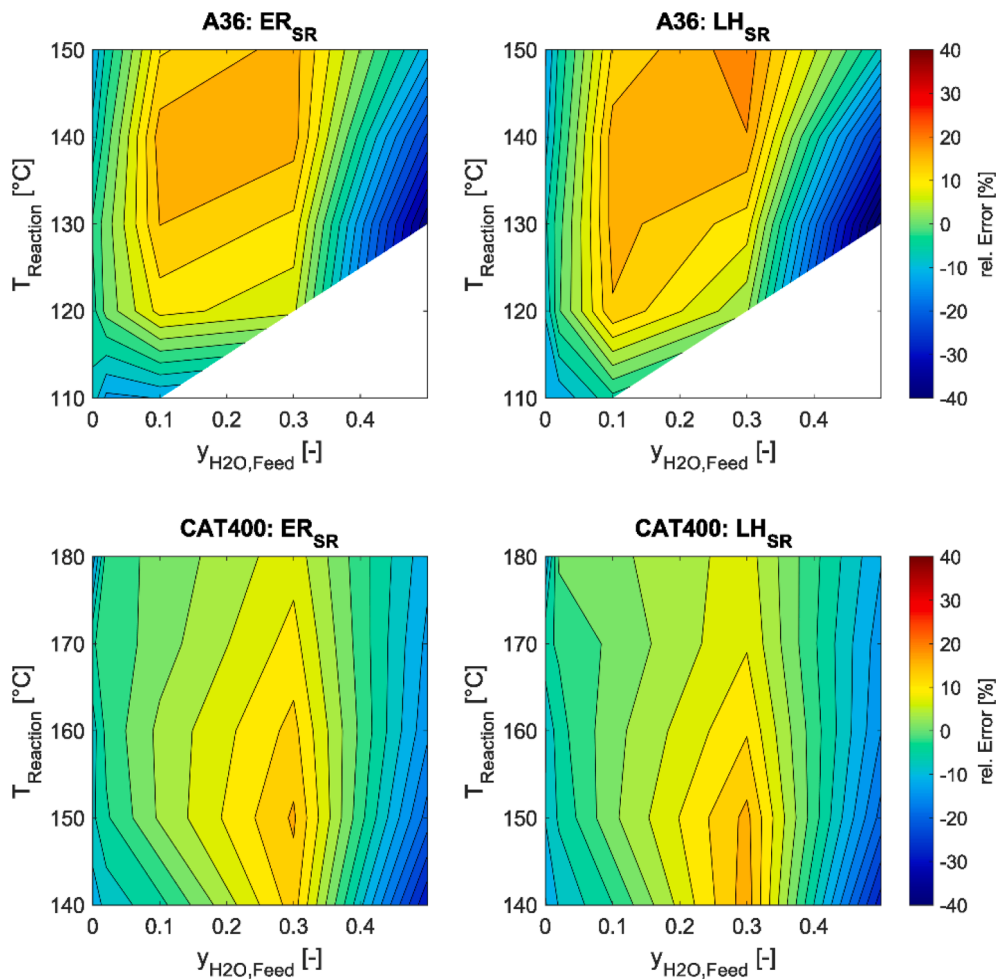


Fig. 8. Relative error of experimental data and simulation data depending on reaction temperature and water fraction of feed. ER_{SR} and LH_{SR} model for A36 (top) and CAT400 (bottom).

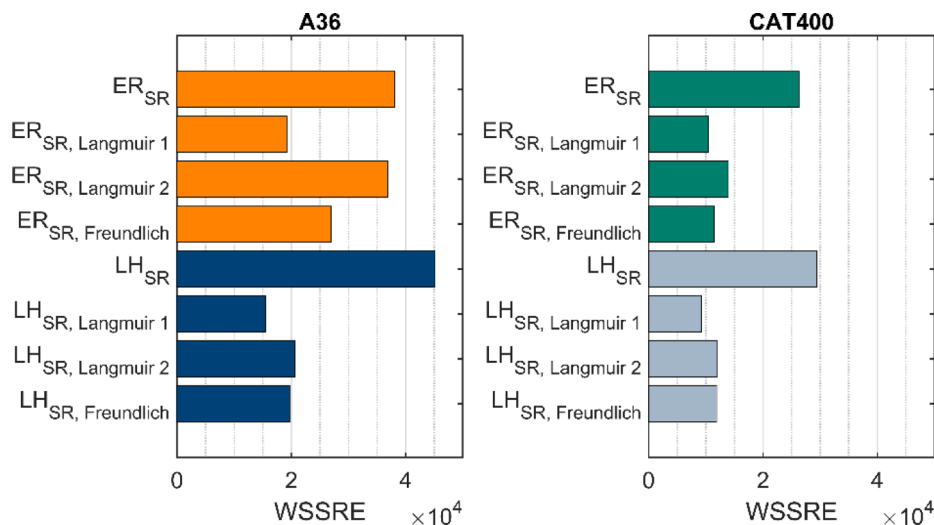


Fig. 9. WSSRE of conventional LH_{SR} and ER_{SR} model and extended models with water inhibition term.

for A36 compared to CAT400. The severe influence of water can be attributed to the selective swelling of ion exchange resins, leading to a highly nonlinear relation between the composition in the bulk phase and the composition at the active sites. In the kinetic studies of Hosseini-najad et al. [15], An et al. [13] and Lei et al. [14] kinetic measurements

were performed only up to water fractions of 0.2. Consequently, the ER or the LH model were found to be appropriately precise by these authors. Extension of the water fractions in the reactor feed considered in this work marks a deficit of both ER and LH to describe the non-linear inhibition effect caused by water. Consequently, a new type of kinetic

Table 9Parameters for the proposed kinetic model $LH_{SR, Langmuir 1}$ for A36 and CAT400.

Parameter	Unit	Proposed kinetic parameter	95 % CI \pm
Amberlyst 36			
k_0	$\text{mol kg}_{\text{Kat}}^{-1} \text{s}^{-1}$	8.089e9	2.284e6
E_A	kJ mol^{-1}	91.56	0.0200
K_{W1}	–	–4.2255	9.733e-4
K_{W2}	K	–2360.9	0.635
Trevelyst CAT400			
k_0	$\text{mol kg}_{\text{Kat}}^{-1} \text{s}^{-1}$	5.973e10	1.135e7
E_A	kJ mol^{-1}	101.98	0.0168
K_{W1}	–	0.4118	1.999e-4
K_{W2}	K	–345.2587	0.756

model is required to allow for a precise kinetic modeling in the whole reactive section of a reactive distillation process, where water mole fractions up to 0.4 are present.

To account for the strong nonlinear inhibitory effect of water both ER_{SR} and LH_{SR} models were extended by the water inhibition term η_w , thereby introducing six new kinetic models, each of which exhibiting two (Langmuir based inhibition terms) or three (Freundlich-based inhibition term) additional fitting parameters, respectively. In principle, the water inhibition term could also be combined with the models with adsorption or desorption as RDS. However, due to the significantly larger error of these models as shown in Fig. 7 and to prevent an exuberant amount of models, these combinations were not further investigated. Fig. 9 shows the resulting WSSRE of the fitted basic and extended models for both catalysts. It can clearly be seen that the extension of the models by a water inhibition term leads to a significant improvement for the LH and ER model in the case of both catalysts. Thereby, the LH model with inhibition term outperforms the ER model with inhibition term for both catalysts.

The $LH_{SR, Langmuir 1}$ model, representing two active sites being blocked by one water molecule represents the best model performing better than all other extended models. Therefore, the $LH_{SR, Langmuir 1}$ model will be used throughout the following discussion. During the fitting procedure of this model, it was found that the ratio of adsorption constants K_{ads} approached a value of zero. Consequently, K_{ads} can be omitted, leading to a simplified rate expression and a reduced number of fitting parameters without compromising the model quality. The corresponding kinetic parameters of the model including 95 % confidence intervals (CI) are shown in Table 9. The model parameters of all other models shown in Fig. 9 are listed in the Supplementary information of this publication. The apparent activation energies are comparable for A36 and CAT400 and were found to be similar to the values discussed in literature [15,39]. The confidence intervals of all four parameters are

small, indicating a strong statistical significance of each parameter.

To compare the performance of the extended kinetic model $LH_{SR, Langmuir 2}$ with the basic model LH_{SR} ones in more detail, Fig. 10 provides the relative error of the experimental and simulation data depending on reaction temperature and water fraction for both catalysts.

The contour plots indicate a significant improvement of the model precision over the whole examined operating range. Especially in the region of high water fractions, a great improvement could be obtained with the extended model $LH_{SR, Langmuir 1}$. The maximum relative error obtained accounts to 15 % (LH_{SR} : 44 %) and 10 % (LH_{SR} : 28 %) for A36 and CAT400, respectively. The slightly higher relative errors for A36 could be attributed to the low absolute conversions at low temperatures, as even small absolute differences then lead to a high relative error.

Fig. 11 compares the measured and simulated conversion profiles for some exemplary operating points for both catalysts investigated in the kinetic study. As expected by the low relative error throughout the operating window, measured and simulated conversion profiles fit very well, regardless of reaction temperature, water fraction or overall conversion.

To illustrate the non-linear inhibition effect of water, Fig. 12 shows the relative reaction rate $\frac{r_{DME}}{r_{DME}(y_{H_2O}=0)}$ at various MeOH-H₂O mixtures calculated based on the extended kinetic model for A36 and CAT400, respectively. Since the initial reaction rate, thus without the presence of formed DME is shown in the graph, the rate equation can be simplified, and the relative reaction rate is equivalent to the water inhibition factor η_w .

For both catalysts, the water inhibition factor decreases sharply at low water fractions and more moderately with increasing water fractions, meaning that small amounts of water inhibit the reaction disproportionately strong. This result is in accordance with the findings of other authors who studied the influence of water on IER catalyzed reactions [35,40,41]. Furthermore, a significant temperature dependence of the water inhibition can be observed, with increasing temperature leading to a less pronounced water inhibition. Consequently, the high-temperature stable CAT400 shows a lower degree of water inhibition in the examined operation range. Regarding an industrial application, this indicates a major advantage in a reactive distillation column, where water is present throughout the reactive zone. Especially in a reactive distillation column using crude MeOH as feedstock this advantage is even more prominent as the average water fraction in the column is in this case even higher.

Fig. 13 compares the proposed extended kinetic model $LH_{SR, Langmuir 1}$ with the existing kinetic models from literature. The parity plot hereby compares the measured conversion from the kinetic study of this work using A36 with the simulated conversion using the respective kinetic

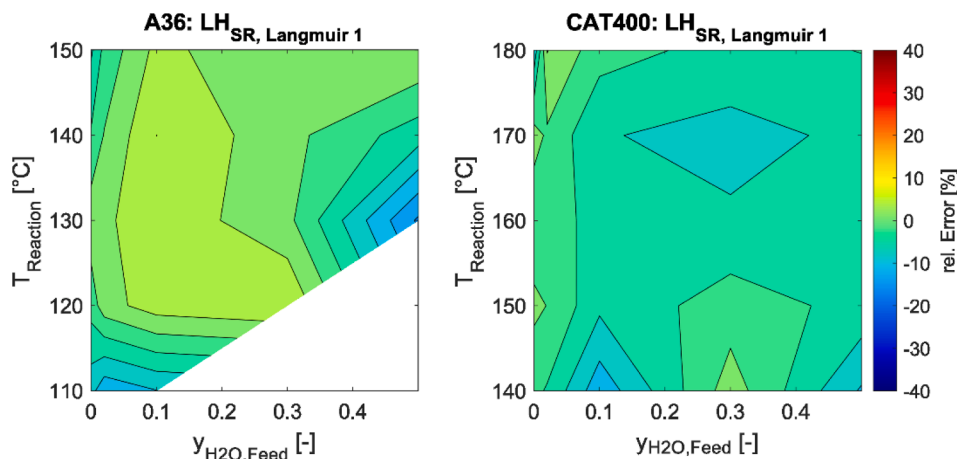


Fig. 10. Relative error of experimental data and simulation data depending on reaction temperature and water fraction of feed. Results for the extended $LH_{SR, Langmuir 1}$ model with water inhibition factor for both catalysts.

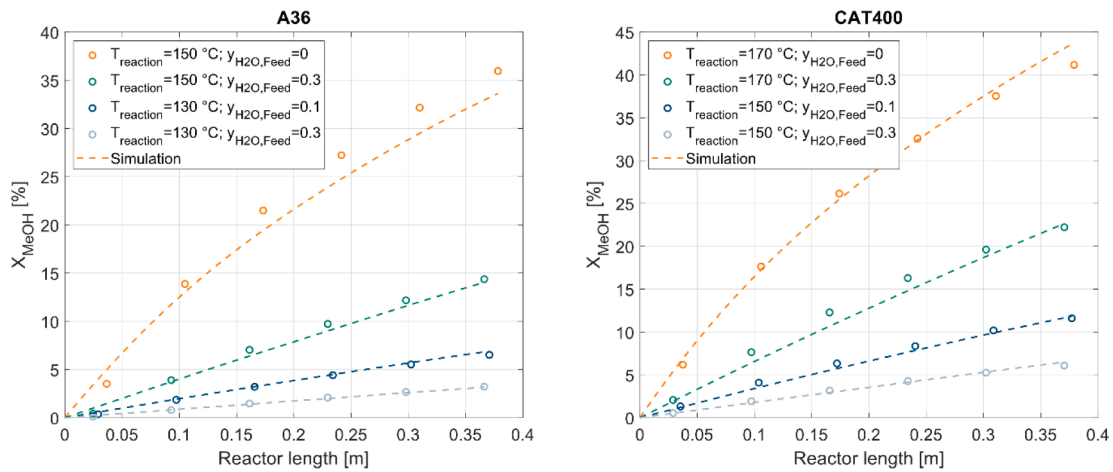


Fig. 11. Measured conversion profiles for exemplary reaction temperatures and feed water fractions for both catalysts. Corresponding simulated conversion profile based on the $LH_{SR, Langmuir 1}$ model.

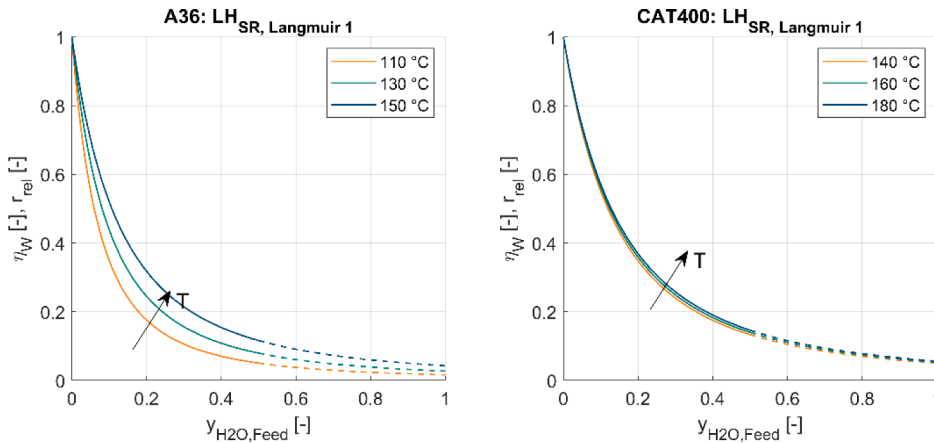


Fig. 12. Inhibition effect of water η_w and relative reaction rate r_{rel} depending on water content and temperature. Relative reaction rate defined as reaction rate at specific water content compared to reaction rate at pure MeOH feed.

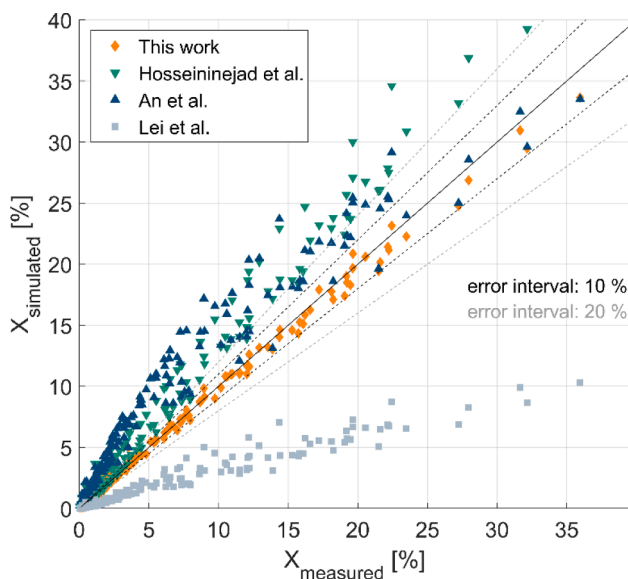


Fig. 13. Parity plot for the MeOH conversion. Experiments were carried out at the profile reactor with A36. Simulations were carried out using kinetic models from literature as published and the $LH_{SR, Langmuir 1}$ model from this work.

model from literature. Hereby it has to be emphasized, that different catalysts are being compared. Amberlyst 35 was used in the work of Hosseinejad et al. and An et al. and an unspecified IER was used in Lei et al. However, due to the similarity in acid capacity of Amberlyst 35 and Amberlyst 36, the authors found a comparison between these different catalysts studies to be useful. The three models from literature show a strong deviation among each other and deviate considerably from the experimental data of this work. The model of Lei et al. reflects much lower conversions throughout the operating window. This result indicates that unspecified IER used in this study exhibited a significantly lower acid capacity than A36. The model proposed by An et al. shows significantly higher conversions at most datapoints, nevertheless, at high conversions, the model is in accordance with the measurements in this work. The best overall agreement from the literature models is achieved with the model of Hosseinejad, however, significant deviations still exist. Yet, considering the small difference in acid capacity between Amberlyst 35 and Amberlyst 36 (5.2 and 5.4 meq/g) the large deviations are surprising. This underlines the significance of the water inhibition term for a kinetic model with wide operating range regarding the water content.

5. Conclusion and outlook

DME is a promising energy carrier in the PtX context with various promising applications. Shifting the reaction from the gas to the liquid

phase enables new process concepts. DME production via reactive distillation leads to a decreased energy demand and reduced process equipment. However, under the moderate reaction temperatures in liquid phase, conventional catalysts show insufficient activity. Consequently, new catalysts are required to enable these intensified process concepts on an industrial scale. In a catalyst screening campaign, two classes of cationic IER, different types of zeolites and perfluorsulfonic acids were tested at 150 °C and – if possible regarding the respective catalysts thermal stability – at 170 °C. During these experiments, the oversulfonated IER A36 and the chlorinated IER CAT400 were identified as the most promising catalysts regarding MeOH conversion and mechanical stability.

Using a profile reactor acquiring both axial temperature and concentration profiles along the reactor, detailed kinetic measurements were conducted for these two catalysts at feed water molar fractions of 0–0.5 and reaction temperatures of 110–150 °C (Amberlyst 36) and 140–180 °C (CAT 400), respectively. Hereby, a significant shrinkage of the catalyst bed due to the distinct swelling behavior of IER could be quantified based on the exothermic heat visible in the fiber optical based high-resolution temperature profile. In the kinetic measurements, the reaction rate has proven to be highly sensitive to the reaction temperature and the water fraction. While at identical temperature CAT400 showed less activity than A36, the higher temperature stability of CAT400 allowed to overcompensate the lower acid capacity, resulting in significantly higher conversions than with A36. Both catalysts showed a reduction of activity over the course of the measurement campaign, indicating that for an industrial long-term application reduced operating temperatures might be required. However, further studies are required to examine the long-term stability under various operating conditions.

The kinetic fitting shows, that both the classical Eley-Rideal or Langmuir-Hinshelwood type kinetic models were unable to describe the strongly non-linear influence of water on the reaction rate sufficiently. For this reason, three different water inhibition terms were introduced to account for the blockage of active sites by water molecules. The water inhibition term based on a Langmuir adsorption isotherm with the assumption that one water molecule blocks two active sites provided the best fitting results. When coupled with the Langmuir-Hinshelwood mechanism, the resulting kinetic model allowed for precise modeling of the reaction rate over the entire measured range for both catalysts investigated in the kinetic study. Furthermore, it was found that the water inhibition is significantly affected by temperature, leading to a lower water inhibition at higher reaction temperatures. For this reason, the chlorinated IER, which was operated at a higher temperature, showed a less pronounced water inhibition compared to the oversulfonated resin.

To the best of our knowledge, the proposed kinetic models offer the highest range of validity of all available kinetic models for the liquid phase MeOH dehydration. Both catalysts considered for the kinetic study in this work were found to be promising candidates for the application in the liquid phase DME synthesis. Due to their different temperature operating windows, the process design of a reactive distillation column is significantly influenced by the catalyst selection. The use of CAT400 enables higher reaction rates and consequently a more compact column design, however the investment cost for a higher column pressure and a heat supply at an increased temperature level should be considered and optimized. The two presented models allow for precise modeling of the reaction kinetics in the operating range of reactive distillation and consequently laying the foundation for a realistic design of DME reactive distillation processes and a profound scientific comparison of both catalysts at process level.

Declaration of Competing Interest

The authors declare that they have no known competing financial interests or personal relationships that could have appeared to influence the work reported in this paper.

Data availability

Data will be made available on request.

Acknowledgements

Deutsche Bundesstiftung Umwelt (DBU) is gratefully acknowledged for funding of the work of Malte Semmel (20020/662).

Special thanks are dedicated to Clariant AG, Chemra GmbH and Puroline GmbH for the supply of the catalysts used in this work.

Appendix A. Supplementary data

Supplementary data to this article can be found online at <https://doi.org/10.1016/j.cej.2022.140525>.

References

- [1] World Energy Council, frontier economics, INTERNATIONAL ASPECTS OF A POWER-TO-X ROADMAP: A report prepared for the World Energy Council Germany 2018 (2018).
- [2] M. Wietschel, L. Zheng, M. Arens, C. Hebling, O. Ranzmeyer, A. Schaadt, C. Hank, A. Sternberg, Herkel, Metastudie Wasserstoff: Auswertung von Energiesystemstudien, 2021.
- [3] K. Ma, Y.e. Tian, Z.-J. Zhao, Q. Cheng, T. Ding, J. Zhang, L. Zheng, Z. Jiang, T. Abe, N. Tsubaki, J. Gong, X. Li, Achieving efficient and robust catalytic reforming on dual-sites of Cu species, *Chem. Sci.* 10 (2019) 2578–2584.
- [4] W. Maus (Ed.), *Zukünftige Kraftstoffe*, Springer, Berlin Heidelberg, Berlin, Heidelberg, 2019.
- [5] T.H. Fleisch, A. Basu, R.A. Sills, Introduction and advancement of a new clean global fuel: The status of DME developments in China and beyond, *J. Nat. Gas Sci. Eng.* 9 (2012) 94–107, <https://doi.org/10.1016/j.jngse.2012.05.012>.
- [6] S.H. Nikos Xydias, LPG-DME Blends Workshop: WLPGA rLPG/rDME Activities, Zurich, 2022.
- [7] M.C. Bauer, A. Kruse, The use of dimethyl ether as an organic extraction solvent for biomass applications in future biorefineries: A user-oriented review, *Fuel* 254 (2019), 115703, <https://doi.org/10.1016/j.fuel.2019.115703>.
- [8] Z. Azizi, M. Rezaeimanesh, T. Tohidian, M.R. Rahimpour, Dimethyl ether: A review of technologies and production challenges, *Chem. Eng. Process. Process Intensif.* 82 (2014) 150–172, <https://doi.org/10.1016/j.cep.2014.06.007>.
- [9] M. Semmel, R.E. Ali, M. Ouda, A. Schaadt, J. Sauer, C. Hebling, Power-to-DME: a cornerstone towards a sustainable energy system, in: G. Spazzafumo (Ed.), *Power to Fuel: How to Speed Up a Hydrogen Economy*, Elsevier, 2021, pp. 123–151.
- [10] T. Cholewa, M. Semmel, F. Mantei, R. Güttel, O. Salem, Process Intensification Strategies for Power-to-X Technologies, *ChemEngineering* 6 (2022) 13, <https://doi.org/10.3390/chemengineering6010013>.
- [11] A.C. Dimian, C.S. Bildea, A.A. Kiss (Eds.), *Applications in Design and Simulation of Sustainable Chemical Processes*, 1st ed., Elsevier, Cambridge, 2019.
- [12] C.S. Bildea, R. György, C.C. Brunchi, A.A. Kiss, Optimal design of intensified processes for DME synthesis, *Comput. Chem. Eng.* 105 (2017) 142–151, <https://doi.org/10.1016/j.compchemeng.2017.01.004>.
- [13] W. An, K.T. Chuang, A.R. Sanger, Dehydration of Methanol to Dimethyl Ether by Catalytic Distillation, Department of Chemical and Materials Engineering, University of Alberta, Edmonton, (2004).
- [14] Z. Lei, Z. Zou, C. Dai, Q. Li, B. Chen, Synthesis of dimethyl ether (DME) by catalytic distillation, *Chem. Eng. Sci.* 66 (2011) 3195–3203, <https://doi.org/10.1016/j.ces.2011.02.034>.
- [15] S. Hosseinienejad, A. Afacan, R.E. Hayes, Catalytic and kinetic study of methanol dehydration to dimethyl ether, *Chem. Eng. Res. Des.* 90 (2012) 825–833, <https://doi.org/10.1016/j.cherd.2011.10.007>.
- [16] M.A. Harmer, Q. Sun, Solid acid catalysis using ion-exchange resins, *Appl. Catal. A Gen.* 221 (2001) 45–62, [https://doi.org/10.1016/S0926-860X\(01\)00794-3](https://doi.org/10.1016/S0926-860X(01)00794-3).
- [17] Fraunhofer ISE, Fraunhofer ISE entwickelt mobilen Teststand für hochaufgelöste Power-to-X-Kinetikanalyse.
- [18] J. Schwarz, D. Samiec (Eds.), B3.4 - Fiber-Optic Measurement of Temperature Profiles. AMA Service GmbH, Von-Münchhausen-Str. 49, 31515 Wunstorf, Germany, 2017.
- [19] F. Nestler, V.P. Müller, M. Ouda, M.J. Hadrich, A. Schaadt, S. Bajohr, T. Kolb, A novel approach for kinetic measurements in exothermic fixed bed reactors: advancements in non-isothermal bed conditions demonstrated for methanol synthesis, *React. Chem. Eng.* 6 (2021) 1092–1107, <https://doi.org/10.1039/D1RE00071C>.
- [20] F. Nestler, M. Krüger, J. Full, M.J. Hadrich, R.J. White, A. Schaadt, Methanol synthesis - industrial challenges within a changing raw material landscape, *Chemie Ingenieur Technik* 90 (2018) 1409–1418, <https://doi.org/10.1002/cite.201800026>.
- [21] M. Baerns, A. Behr, A. Brehm, J. Gmehling, K.-O. Hinrichsen, H. Hofmann, R. Palkovits, U. Onken, A. Renken, *Technische Chemie*, second. Auflage, Wiley-VCH Verlag GmbH & Co. KGaA, Weinheim, 2013.
- [22] J. Lilja, J. Aumo, T. Salmi, D. Murzin, P. Mäki-Arvela, M. Sundell, K. Ekman, R. Peltonen, H. Vainio, Kinetics of esterification of propanoic acid with methanol

- over a fibrous polymer-supported sulphonic acid catalyst, *Appl. Catal. A Gen.* 228 (2002) 253–267, [https://doi.org/10.1016/S0926-860X\(01\)00981-4](https://doi.org/10.1016/S0926-860X(01)00981-4).
- [23] M. Kraume (Ed.), *Transportvorgänge in Der Verfahrenstechnik*, Springer Berlin Heidelberg, Berlin, Heidelberg, 2012.
- [24] J. Voggenreiter, A. Ferre, J. Burger, Scale-up of the Continuous Production of Poly (oxymethylene) Dimethyl Ethers from Methanol and Formaldehyde in Tubular Reactors, *Ind. Eng. Chem. Res.* 61 (2022) 10034–10046, <https://doi.org/10.1021/acs.iecr.2c01468>.
- [25] DIPPR, Thermophysical Properties Laboratory Project 801, 2009. <http://dippr.byu.edu/> (accessed 29 February 2016).
- [26] VDI-Gesellschaft Verfahrenstechnik und Chemieingenieurwesen, *VDI-Wärmeatlas*, Springer, Berlin Heidelberg, Berlin, Heidelberg, 2013.
- [27] C.C. Li, Thermal conductivity of liquid mixtures, *AIChE J.* 22 (1976) 927–930, <https://doi.org/10.1002/aic.690220520>.
- [28] C.R. Wilke, P. Chang, Correlation of diffusion coefficients in dilute solutions, *AIChE J.* 1 (1955) 264–270, <https://doi.org/10.1002/aic.690010222>.
- [29] G.F. Froment, K.B. Bischoff, J. de Wilde, *Chemical Reactor Analysis and Design*, thirdrd Edition, John Wiley & Sons Inc, 2011.
- [30] R. Soto, C. Fité, E. Ramírez, M. Iborra, J. Tejero, Catalytic activity dependence on morphological properties of acidic ion-exchange resins for the simultaneous ETBE and TAE liquid-phase synthesis, *React. Chem. Eng.* 3 (2018) 195–205, <https://doi.org/10.1039/c7re00177k>.
- [31] R. Tesser, M. Di Serio, L. Casale, L. Sannino, M. Ledda, E. Santacesaria, Acid exchange resins deactivation in the esterification of free fatty acids, *Chem. Eng. J.* 161 (2010) 212–222, <https://doi.org/10.1016/j.cej.2010.04.026>.
- [32] E. van de Steene, J. de Clercq, J.W. Thybaut, Ion-exchange resin catalyzed transesterification of ethyl acetate with methanol: Gel versus macroporous resins, *Chem. Eng. J.* 242 (2014) 170–179, <https://doi.org/10.1016/j.cej.2013.12.025>.
- [33] A. Jess, P. Wasserscheid, *Chemical technology: An integral textbook*, Wiley-VCH, Weinheim, 2013.
- [34] Elizabeth Louisa du Toit, The rate inhibiting effect of water as a product on reactions catalysed by cation exchange resins: Formation of mesityl oxide from acetone as a case study. Dissertation, Pretoria, 2003.
- [35] M.Á. Pérez-Maciá, R. Bringué, M. Iborra, J. Tejero, F. Cunill, Kinetic study of 1-butanol dehydration to di-n-butyl ether over Amberlyst 70, *AIChE J.* 62 (2016) 180–194, <https://doi.org/10.1002/aic.15020>.
- [36] J.C. Lagarias, J.A. Reeds, M.H. Wright, P.E. Wright, Convergence Properties of the Nelder-Mead Simplex Method in Low Dimensions, *SIAM J. Optim.* 9 (1998) 112–147, <https://doi.org/10.1137/S1052623496303470>.
- [37] E. Catizzone, G. Bonura, M. Migliori, F. Frusteri, G. Giordano, CO₂ recycling to dimethyl ether: state-of-the-art and perspectives, *Molecules* 23 (2017), <https://doi.org/10.3390/molecules23010031>.
- [38] X. Sun, Y. Yang, Y. He, S. Zhu, Z. Liu, Stability of Zeolite HZSM-5 in Liquid Phase Dehydration of Methanol to Dimethyl Ether, *Catal. Lett.* (2020), <https://doi.org/10.1007/s10562-020-03454-y>.
- [39] P.K. Kiviranta-Pääkkönen, L.K. Struckmann, J.A. Linnekoski, A.O.I. Krause, Dehydration of the Alcohol in the Etherification of Isoamylenes with Methanol and Ethanol, *Ind. Eng. Chem. Res.* 37 (1) (1998) 18–24.
- [40] T. Baba, Y. Ono, Kinetic studies in liquid phase dehydration-cyclization of 1,4-butanediol to tetrahydrofuran with heteropoly acids, *J. Mol. Catal.* 37 (1986) 317–326, [https://doi.org/10.1016/0304-5102\(86\)85020-9](https://doi.org/10.1016/0304-5102(86)85020-9).
- [41] U. Limbeck, C. Altwicker, U. Kunz, U. Hoffmann, Rate expression for THF synthesis on acidic ion exchange resin, *Chem. Eng. Sci.* 56 (2001) 2171–2178, [https://doi.org/10.1016/S0009-2509\(00\)00497-8](https://doi.org/10.1016/S0009-2509(00)00497-8).